Environ Fluid Mech (2011) 11:329–352
DOI 10.1007/s10652-011-9209-0

ORIGINAL ARTICLE

Numerical modeling of aquaculture dissolved waste transport in a coastal embayment

Subhas K. Venayagamoorthy · Hyeyun Ku · Oliver B. Fringer · Alice Chiu · Rosamond L. Naylor · Jeffrey R. Koseff

Received: 2 November 2009 / Accepted: 20 January 2011 / Published online: 18 February 2011
© Springer Science+Business Media B.V. 2011

Abstract Marine aquaculture is expanding rapidly without reliable quantification of effluents. The present study focuses on understanding the transport of dissolved wastes from aquaculture pens in near-coastal environments using the hydrodynamics code SUNTANS (Stanford Unstructured Nonhydrostatic Terrain-following Adaptive Navier–Stokes Simulator), which employs unstructured grids to compute flows in the coastal ocean at very high resolution. Simulations of a pollutant concentration field (in time and space) as a function of the local environment (bathymetry), flow conditions (tides and wind-induced currents), and the location of the pens were performed to study their effects on the evolution of the waste

S. K. Venayagamoorthy (✉) · H. Ku
Department of Civil and Environmental Engineering, Colorado State University, Fort Collins, CO 80523-1372, USA
e-mail: vskaran@colostate.edu

H. Ku
e-mail: hyeyun@engr.colostate.edu

O. B. Fringer · J. R. Koseff
Environmental Fluid Mechanics Laboratory, Department of Civil and Environmental Engineering, Stanford University, Stanford, CA 94305, USA

O. B. Fringer
e-mail: fringer@stanford.edu

J. R. Koseff
e-mail: koseff@stanford.edu

A. Chiu · R. L. Naylor
Program on Food Security and the Environment, Stanford University, Stanford, CA 94305, USA

A. Chiu
e-mail: alchiu@stanford.edu

R. L. Naylor
e-mail: roz@stanford.edu

O. B. Fringer · R. L. Naylor · J. R. Koseff
Woods Institute for the Environment, Stanford University, Stanford, CA 94305-4205, USA

plume. The presence of the fish farm pens cause partial blockage of the flow, leading to the deceleration of the approaching flow and formation of downstream wakes. Results of both the near-field area (area within 10 to 20 pen diameters of the fish-pen site) as well as far-field behavior of the pollutant field are presented. These detailed results highlight for the first time the importance of the wake vortex dynamics on the evolution of the near-field plume as well as the rotation of the earth on the far-field plume. The results provide an understanding of the impact of aquaculture fish-pens on coastal water quality.

Keywords Effluent pollution · Dispersion · Aquaculture · Numerical modeling · Plume dynamics · Coastal engineering

1 Introduction

The rapid expansion of marine aquaculture is a potential solution to the problem of overfishing and fisheries depletion worldwide, but also a major threat to ocean ecosystems. One of the most widely cited but poorly quantified impacts of open netpen aquaculture is its release of nutrients and other wastes to the surrounding environment [14]. In the United States there is considerable pressure on state and federal agencies to regulate the growth and mitigate the impacts of aquaculture operations in coastal waters [13]. In May 2006, the California legislature passed the California Sustainable Oceans Act (SOA) to establish regulations that ensure marine finfish aquaculture operations in state waters are environmentally sustainable (see Box 1). The framework for evaluating environmental impacts and proper siting of aquaculture facilities is expected to be certified by the Department of Fish and Game by the fall of 2011. However, there remains much uncertainty regarding the environmental impacts of aquaculture operations and the appropriate (and reliable) methods for regulating these impacts. The goal of this study is to adapt and employ a highly-resolved numerical modeling tool that will allow the user to predict the impact of a particular aquaculture operation on water quality in a coastal environment. In particular, we seek to answer the questions: Where and in what concentrations will the dissolved waste from aquaculture pens located in near-shore and off-shore environments be found, and what will the impact be on water quality?

Proper assessment of the potential impact of a fish farm with several pens is closely linked to the mixing and dispersal of the waste discharge from the pens with the ambient flow [9]. The dispersal of wastes from pens released into the coastal ocean may not be necessarily "Gaussian" (monotonically decreasing from the source in all directions) and therefore 'dilution may *not* be the solution' contrary to what is often claimed. The evidence from previous laboratory and field studies [5,19] suggests that wastes may be transported in plumes that retain their coherence and maintain relatively high concentrations over large distances. This pattern of dispersal could result in much higher concentrations of wastes at certain points on the coastline, even at considerable distances from the source.

There is very little work in the refereed literature describing the dispersal of aquaculture wastes under varying hydrodynamic conditions at the field scale. Previous numerical studies have focused mostly on the near-field mixing under steady uni-directional flow conditions [9]. Some recent field measurements on mussel and shellfish aquaculture identify the environmental impacts of large farms which include wave attenuation and flow suppression due to interaction with stratification [6,15,20]. The complex nature of the flow around fish pens is caused by flow separation due to partial blockage of the flow by the pens and the combined

effects of tides and winds. At larger scales, the influence of the earth's rotation becomes important and can alter the evolution of the waste plume considerably.

Using representative field-scale physical and flow parameter values in our model, we are able to address a number of policy-relevant issues. For example, the model can assist with siting decisions by taking into account local currents and flow conditions to identify locations where dissolved wastes could negatively impact other users, public trust values, or the marine environment (factor 1 in Box 1). Knowing the spatial distribution of effluents emitted from a net pen allows one to better understand the effects of that pen on sensitive habitats, ecosystems, other uses, and plant and animal species, including marine mammals and birds, in the vicinity (factors 2, 3, 4, 6 in Box 1). The modeling technique can be most directly applied to factor number 5 in determining the extent and concentration of a variety of products, pollutants, and nutrient wastes over space and time. Future development of the model may also lend insight to the interactions among effluents from several farms sited together (i.e., cumulative effects as mentioned in factor 7). While certainly not a substitute for on-the-ground monitoring, the effluent model can be a useful tool for predicting a site's ability to meet water quality standards before aquaculture operations are established. The model allows a potential aquaculture operator to provide a more accurate description of the expected discharge(s) from their facility in the Notice of Intent submitted to the water boards [3].

Box 1: PEIR requirements as set out in the California Sustainable Oceans Act (SOA). The first step in implementing the SOA is the preparation of a programmatic environmental impact report (PEIR), which is currently being drafted. The Act describes the purpose of the PEIR: *…the report shall provide a framework for managing marine finfish aquaculture in an environmentally sustainable manner that, at a minimum, adequately considers all of the following factors:*

1. *Appropriate areas for siting marine finfish aquaculture operations to avoid adverse impacts, and minimize any unavoidable impacts, on user groups, public trust values, and the marine environment.*
2. *The effects on sensitive ocean and coastal habitats.*
3. *The effects on marine ecosystems, commercial and recreational fishing, and other important ocean uses.*
4. *The effects on other plant and animal species, especially species protected or recovering under state and federal law.*
5. *The effects of the use of chemical and biological products and pollutants and nutrient wastes on human health and the marine environment.*
6. *The effects of interactions with marine mammals and birds.*
7. *The cumulative effects of a number of similar finfish aquaculture projects on the ability of the marine environment to support ecologically significant flora and fauna.*
8. *The effects of feed, fish meal, and fish oil on marine ecosystems.*
9. *The effects of escaped fish on wild fish stocks and the marine environment.*
10. *The design of facilities and farming practices so as to avoid adverse environmental impacts, and to minimize any unavoidable impacts.*
(California F&GC Code [2]).

While policy applications are the end goal, our initial focus, and the focus of this paper, is simpler. We are modeling the dispersal of "dissolved wastes" (considered here as passive scalars) such as nitrogen and phosphorus from aquaculture pens using high-resolution, two-dimensional, depth-averaged numerical simulations under different time-varying flows in an idealized coastal embayment. We highlight the different dispersal patterns that may occur under various forcing scenarios (flows, tides, earth's rotation, and local sources) in a more idealized model bathymetry. The layout of this paper is as follows: In Sect. 2, we briefly describe the computational approach we employ for this study, provide an overview of the problem set-up and outline a summary of all the simulation cases that will be discussed in Sect. 3. We then present and discuss results of the lateral mixing of a continuous pollutant source emanating from single pen in a channel flow as well as from an array of aquaculture pens in a idealized coastal embayment under different flow conditions in Sect. 3. Finally we draw some conclusions and provide some directions for future work in Sect. 4.

2 Numerical methodology and problem configuration

2.1 Numerical methodology

We employ the SUNTANS code developed by Fringer et al. [8] to perform highly resolved simulations of flow through and around fish pens in the idealized coastal embayment shown in Fig. 1. SUNTANS is an unstructured, finite-volume, parallel coastal-ocean simulator that solves the three-dimensional nonhydrostatic Navier–Stokes equations with the Boussinesq approximation in a rotating frame. It also solves for the free surface as well as the transport of salinity and temperature (see Fringer et al. [8] and Wang et al. [21] for details). This code has been applied to a host of coastal problems and processes such as the generation and evolution of internal waves in Monterey Bay [11] and the South China Sea [22] and high-resolution simulations of estuarine hydrodynamics [21]. However, in this study, we use the depth-averaged formulation of SUNTANS using a single vertical layer for all the simulations. Hence, the governing equations revert to the two-dimensional shallow water equations (also known as the Saint-Venant equations), together with the depth-averaged continuity equation given by

$$\frac{\partial u}{\partial t} + u\frac{\partial u}{\partial x} + v\frac{\partial u}{\partial y} - fv = -g\frac{\partial h}{\partial x} + \nu_H\left(\frac{\partial^2 u}{\partial x^2} + \frac{\partial^2 u}{\partial y^2}\right) + \frac{\tau_x^s}{H} - C_{DB}\frac{\sqrt{u^2+v^2}}{H}u + F_{D,x}, \tag{1}$$

$$\frac{\partial v}{\partial t} + u\frac{\partial v}{\partial x} + v\frac{\partial v}{\partial y} + fu = -g\frac{\partial h}{\partial y} + \nu_H\left(\frac{\partial^2 v}{\partial x^2} + \frac{\partial^2 v}{\partial y^2}\right) + \frac{\tau_y^s}{H} - C_{DB}\frac{\sqrt{u^2+v^2}}{H}v + F_{D,y}, \tag{2}$$

$$\frac{\partial h}{\partial t} + \frac{\partial}{\partial x}(Hu) + \frac{\partial}{\partial y}(Hv) = 0, \tag{3}$$

where $H = h + d$ is the total water depth in m, h is the free-surface height relative to some vertical datum in m, d is the depth of the bottom relative to some vertical datum in m, u, v are the horizontal cartesian components of the depth-averaged velocity vector in m s^{-1}, t is time in s, g is the constant of gravitational acceleration in m s^{-1}, $f = 2\Omega_{earth}\sin\phi_{lat}$ is

the Coriolis parameter with Ω_{earth} been the angular velocity of the earth's rotation in s^{-1} and ϕ_{lat} the latitude, ν_h is the horizontal eddy viscosity in $m^2\ s^{-1}$, τ_x^s and τ_y^s are the free-surface stresses at $z = h$, C_{DB} is a non-dimensional bottom drag coefficient and $F_{D,x}$ and $F_{D,y}$ are the pen-induced drag forces in the x and y directions respectively, and are given by a quadratic drag law formulation as shown in (5).

We opted to use the two-dimensional depth-averaged formulation since this study is a first step in addressing far-field influence of the near-field dynamics, with a particular emphasis on the near-field vortex street which is predominantly two-dimensional. Furthermore, the two-dimensional highly resolved simulations on their own are computationally intensive and therefore three-dimensional simulations and associated parameter studies were not feasible due to computational and time constraints for the scope of work we have performed using the two-dimensional simulations.

2.2 Problem configuration

The domain we use for the main part of this study is a model coastal embayment that is 10 km in length and 5 km wide as shown in Fig. 1. The bathymetry of the domain consists of a shallow embayment incised by a deep channel as shown in Fig. 2. Two sets of 6 20 m diameter fish pens are used in this study, as shown in Fig. 1, and the fish pens are all located close to the western edge of the embayment. We present results showing the effect of varying the location of the pens on the dispersal of the waste plume in Sect. 3.

At the alongshore boundaries of the domain shown in Fig. 1, we impose a velocity field of the form

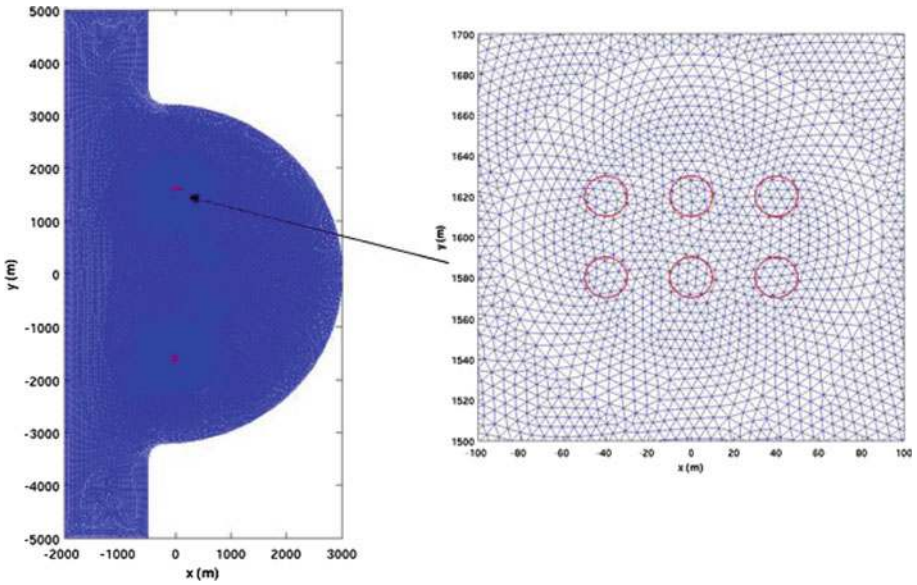

Fig. 1 Unstructured computational mesh showing the embayment used in the simulations for this study. A velocity field described by Eq. 4 is imposed at the northern boundary of the domain with a M_2 tidal frequency of 1.4×10^{-4} rad s^{-1}. The image on the right shows a zoomed view highlighting the grid refinement around an array of six 20 m diameter pens

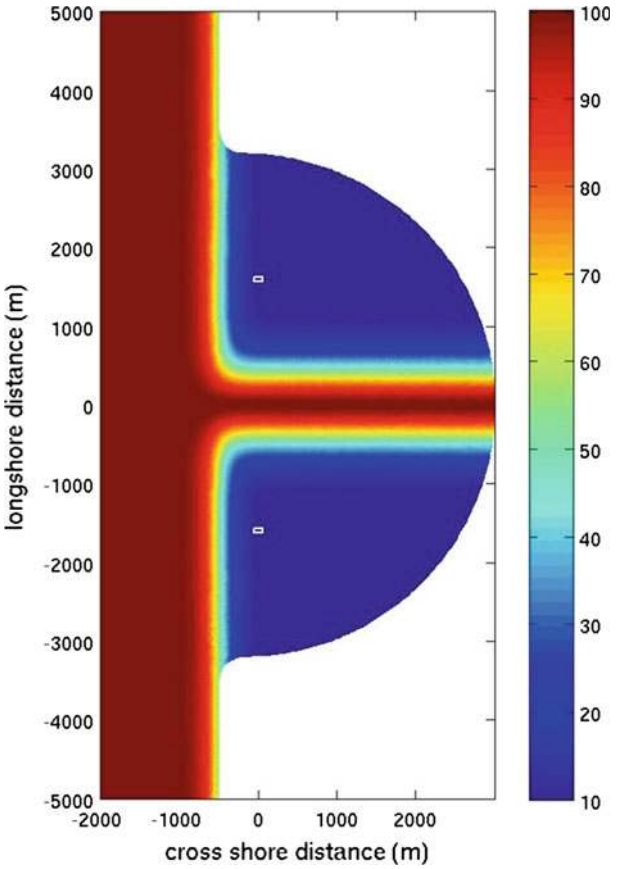

Fig. 2 Idealized depth contours of the model embayment depicting a shallow shelf incised by a deep channel. Locations of model fish pens are depicted by the white boxes (for the offshore cases listed in Table 1). The depth is indicated by the *color bar* in meters

$$v = U_m + U_T \sin(\omega t), \tag{4}$$

where $U_m \leq 0$ is the amplitude of the mean current (where flow is in the north-south direction); U_T is the amplitude of the sinusoidal tidal component of the flow field with forcing frequency ω; and v is the alongshore component of the velocity field. Boundary conditions for the horizontal velocity v are free-slip along the coastline and offshore boundary. The horizontal component in the x-direction of the velocity field u has no-flux boundary conditions along the coastline and the offshore boundary. The scalar field has no-flux boundary conditions on all boundaries. An unstructured mesh is generated for this study with a total of approximately 162,500 cells, with grid refinement in the vicinity of the fish pens as shown in Fig. 1. The resolution near the pens is roughly 5 m, while that in the far-field is stretched to 50 m. Each individual fish pen is cylindrical in shape with a diameter of $D = 20$ m. A drag law formulation is employed to account for the flow reduction inside the pens and the resulting decrease in momentum downstream of the pens. This drag formulation is given by a quadratic drag-law on the right-hand side of the x- and y-momentum equations shown in (1) and (2) and are of the form

$$F_{D,x} = -\frac{\alpha C_D (u^2 + v^2)^{1/2}}{D} u,$$
$$F_{D,y} = -\frac{\alpha C_D (u^2 + v^2)^{1/2}}{D} v, \tag{5}$$

where C_D is the non-dimensional drag coefficient exerted by the fish pens, u and v are the Cartesian components of the velocity vector, and $\alpha = 1$ inside of the pens while $\alpha = 0$ outside of the pens. We use a horizontal eddy-viscosity of $\nu_h = 10^{-3}\,\mathrm{m^2\,s^{-1}}$, and a quadratic bottom drag law formulation (as shown in (1) and (2)) with a drag coefficient of $C_{D,bottom} = 0.0025$. An estimate of the Reynolds number based on a characteristic velocity scale of $0.1\,\mathrm{m\,s^{-1}}$ and the specified values of $D = 20\,\mathrm{m}$ and $\nu_h = 10^{-3}\mathrm{m^2\,s^{-1}}$ is $Re = 2000$. A continuous pollutant (scalar) point source is placed inside the perimeter of each pen as an approximation of the effluent waste discharged from the pens. No horizontal scalar diffusivity is employed since it is assumed that transport dominates the dispersion. Transport is computed with a high-resolution total variation diminishing (TVD) scheme, as implemented by Zhang and Fringer [22]. The TVD scheme is explicit and hence conditionally stable but it guarantees monotonicity. For all simulations, we restrict the time step such that the maximum Courant number, based on the smallest grid spacing and the maximum currents, is roughly 0.5. This provides sufficient temporal resolution while maintaining stability.

An important non-dimensional parameter for the simple model flow problem defined by (4) is the ratio of the tidal to mean flow given by

$$\eta = \frac{U_T}{U_m}, \tag{6}$$

which compares the amplitude of the oscillatory flow to the amplitude of the mean current and is an important parameter that determines the shape of the contaminant plume [16]. A second important parameter is the non-dimensional tidal excursion lengthscale given by

$$K = \frac{2U_T}{\omega D}, \tag{7}$$

where U_T is the amplitude of the tidal current, ω is the forcing frequency and D is the pen diameter. This represents the ratio of the tidal excursion to the pen diameter and is analogous to the Keulegan-Carpenter number used in wave-structure interaction studies. For all of the simulations performed in this study, we have used an alongshore velocity magnitude of $U_m = 0.1\,\mathrm{m\,s^{-1}}$, which is representative of mean currents in coastal regions such as the St. Lawrence Island in the Bering Sea. The tidal velocity magnitude is varied to yield different (field-scale) values of η and K. In Sect. 3, we discuss the influence of these and other parameters on the dispersion of a contaminant plume in the idealized coastal embayment shown in Fig. 1.

2.3 Simulation cases

We performed a total of 11 simulations for this study as shown in Table 1. The first four simulations (cases 1 through 4) are used as test cases to show the transverse mixing of a plume around a cylindrical 20 m diameter pen in a rectangular open channel that is 3 km long and 1 km wide. Case 1 will be used to highlight the classical Gaussian behavior of the plume in a uni-directional flow in the absence of rotation and without pen-induced drag ($C_D = 0$) and validate the numerical model results with analytical/empirical results of plume dynamics. Cases 2 and 3 are also uni-directional channel flow cases with pen-induced drag

Table 1 Summary of the 11 cases simulated in the present paper. The last column provides some remarks where the Rossby number ($Ro = U_m/(fL)$, where $L = 5$ km) and other variables and/or comments are shown

Case #	Case name	Domain	C_D	η	K	Remarks
1	Steady flow	Channel	0	0	0	$Ro = \infty$
2	Steady flow	Channel	0.5	0	0	$Ro = \infty$
3	Steady flow	Channel	1.0	0	0	$Ro = \infty$
4	Uniform + Oscillating flow	Channel	1.0	1	46	$Ro = \infty$
5	Offshore base case	Embayment	1.0	1	71	$Ro = 0.26$
6	Offshore with no rotation	Embayment	1.0	1	71	$Ro = \infty$
7	Offshore with river inflow	Embayment	1.0	1	71	$U_R/U_m = 0.5$
8	Offshore with no pen drag	Embayment	0	1	71	$Ro = 0.26$
9	Nearshore base case	Embayment	1.0	1	71	$Ro = 0.26$
10	Nearshore with strong tides	Embayment	1.0	2	71	$Ro = 0.26$
11	Nearshore with wind	Embayment	1.0	∞	71	$u_{10} = 10\ \mathrm{m\ s^{-1}}$

coefficients $C_D = 0.5$ and 1, respectively. These two cases will be used to demonstrate the effects of the drag force induced by a pen on the lateral mixing of the plume and to provide a measure of the model sensitivity on C_D. Case 4 is presented to highlight the added effect of tidal oscillation (with $\eta = 1$, $K = 46$ and $C_D = 1$) compared to case 3 (with $\eta = 0$, $K = 0$ and $C_D = 1$).

The remaining seven simulations are of the coastal embayment shown in Fig. 1 for different flow conditions and locations. Case 5, which we refer to as the 'offshore base case', takes into account the drag induced by each of the 12 pens with $C_D = 1$. We have also included the earth's rotation with a Coriolis parameter of $f = 8.7 \times 10^{-5}$ rad s^{-1}. The flow field is driven by a tidal flow from north to south combined with a southerly flowing mean current as described by (4). The relevant oscillating flow parameters are $\eta = 1$ and $K = 71$, based on a tidal velocity amplitude of $U_T = 0.1\ \mathrm{m\ s^{-1}}$ and M_2 tidal period of 12.42 h.

Case 6 shows a similar simulation to case 5 except that here, the Coriolis terms in the momentum equations ((1) and (2)) were switched off by simply setting $f = 0$. Case 7 presents a simulation where we have added a river inflow to case 5, with all other parameters kept identical to case 5. A small river inflow river discharge with a velocity of $U_R = 0.05\ \mathrm{m\ s^{-1}}$ was placed symmetrically at the channel incision at the central embayment coast (i.e. at a alongshore distance of 0 m). The width of the river inflow is 400 m and the discharge is approximately $1500\ \mathrm{m^3\ s^{-1}}$. This is about 10% of the volume flow rate entering the embayment from the northern alongshore boundary from the mean and tidally-induced flow. Case 8 is a simulation where the pen-induced drag is switched off ($C_D = 0$) with all other parameter kept identical to the 'offshore base case' (case 5).

Case 9 is what we refer to as the 'nearshore base case' in Table 1. Our goal here is to explore the variability in the plume dispersion as a function of the location of the pens. A whole range of scenarios are possible and would be prohibitively expensive to completely simulate computationally. Here, the southern facing farm in Fig. 1 was moved into the bay and closer to the channel incision (see Fig. 15). All other conditions remain unchanged relative to the 'offshore base case'. Case 10 is also a nearshore simulation (where the pens are in the same locations as case 9) with a stronger tidal signal ($\eta = 2$) compared to the 'nearshore base case' where $\eta = 1$. As discussed earlier in Sect. 2.2, η influences the shape of the

plume. When $\eta > 1$, plume reversals will occur and dramatic changes to the plume structure can be expected. Case 11 presents a nearshore simulation where surface wind stress acts over the entire embayment in a northerly direction (i.e. opposite to the tidal flow). We have also removed the mean current for this case in order to explore the effect of the wind-induced circulation on the plume distribution.

It is important to note that the point of these simulations is not to perform a parameter study to investigate the quantitative effects of a single parameter on the dispersion, but rather to demonstrate the pronounced variability of the contaminant plume and how it is highly sensitive to different environmental forcing scenarios.

2.4 Statistical parameters for assessing plume distribution

Statistical indicators such as moments of non-dimensional plume concentration can provide quantitative information on the plume characteristics. We compute the moments of the alongshore concentration distributions i.e. the mean, standard deviation, skewness, and kurtosis for all the embayment cases (cases 5–11). Here, we provide a description of these key statistical parameters that will be used for discussing the alongshore plume distribution in Sect. 3.

The standard deviation provides an indication of spread (or dispersion) of a distribution and is defined as the root-mean-square of the concentration values (also defined as the square root of the variance) from their mean and given by

$$\sigma = \sqrt{m_2} = \sqrt{\frac{\sum_{j=1}^{N} \left(C_j - \overline{C}\right)^2}{N}}, \tag{8}$$

where $\overline{C}$ is the mean of the concentration distribution, N is the sample size and m_2 is the variance or the second moment about the mean. The skewness provides an indication of the degree of asymmetry of a distribution when compared to the perfectly symmetrical Gaussian distribution and is defined as the third moment about the mean normalized by the cube of the standard deviation (see Eq. 9), while the kurtosis provides a measure of peakedness of a distribution usually taken relative to a Gaussian distribution (noting that a Gaussian distribution has a kurtosis of 3) and is given by the fourth moment about the mean divided by the variance (see Eq. 10). A concentration distribution with large kurtosis indicates strong intermittency while a distribution with large skewness indicates a highly asymmetrical distribution.

$$\gamma = \frac{m_3}{\sqrt{m_2^3}} = \frac{\frac{1}{N}\sum_{j=1}^{N} \left(C_j - \overline{C}\right)^3}{\left(\frac{1}{N}\sum_{j=1}^{N} \left(C_j - \overline{C}\right)^2\right)^{3/2}}, \tag{9}$$

$$\beta = \frac{m_4}{m_2^2} = \frac{\frac{1}{N}\sum_{j=1}^{N} \left(C_j - \overline{C}\right)^4}{\left(\frac{1}{N}\sum_{j=1}^{N} \left(C_j - \overline{C}\right)^2\right)^2}. \tag{10}$$

3 Results and discussion

In this section, we first present results from the channel flow test cases (cases 1 through 4) to show the lateral mixing of a plume around a cylindrical fish pen in a rectangular channel. The goal is to highlight the classical behavior of the plume and the enhanced mixing that occurs due to vortices introduced by flow separation around a fish pen. We then focus our

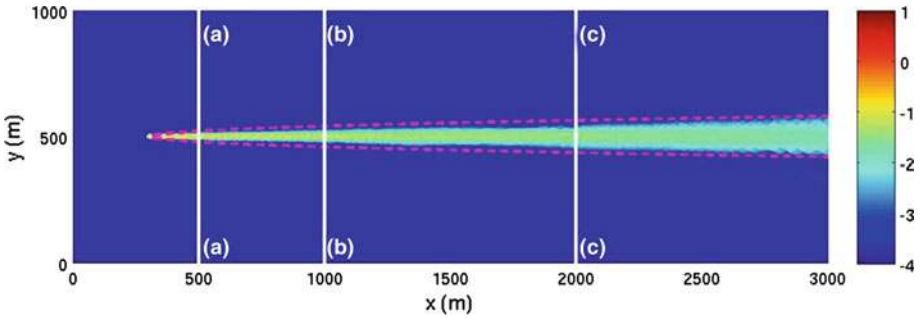

Fig. 3 Time-averaged normalized concentration field (shown in color) for a steady uni-directional test flow case (case 1 in Table 1). The *dashed red line* shows the classical spread of a Gaussian plume using a lateral diffusivity of $0.03\,\mathrm{m^2\,s^{-1}}$

attention mainly on the discussion of the simulation results of the coastal embayment under different flow conditions and pen locations (simulation cases 5 through 11).

3.1 Channel cases (cases 1 through 4)

We performed a series of two-dimensional, depth-averaged simulations in an idealized rectangular channel for a wide parameter space in C_D, K and η to investigate their effects on dispersion. Here we present results and discussion to provide validation for our numerical model with a well known empirical relationship for the transverse (lateral) mixing coefficient, and to highlight the enhanced mixing caused by the pen-induced drag compared to the classical dispersion (case 1).

The time-averaged non-dimensional concentration (hereafter concentration will be used to imply non-dimensional concentration) field for the steady uni-directional channel flow case (case 1) is shown in Fig. 3. The spanwise concentration distributions at sections (a–a), (b–b) and (c–c) are shown in Fig. 4, respectively. The dashed red line in Fig. 3 shows the classical spread of the plume width using an empirical lateral mixing coefficient $\epsilon_t/(du^*) = 0.15$, where d is the water depth and u^* is the shear velocity [7,12]. It should be noted that the nondimensional lateral mixing coefficient was in the range of 0.1–0.2 in the experiments and hence 0.15 is considered as an average value. It is well known from experiments [1,7,12] and direct numerical simulations of channel flows (see for example Hoyas and Jimenez [10]) that the mean velocity U is approximately $25u^*$. Using this relationship, gives a value for $\epsilon_t = 0.03\,\mathrm{m^2\,s^{-1}}$. This is in good agreement with the lateral diffusivity of $0.026\,\mathrm{m^2\,s^{-1}}$ computed from the variances of the concentration distributions shown in Fig. 4. It can be seen from Fig. 3 that the $x^{1/2}$ growth for the plume width predicted by the Gaussian formulation agrees reasonably well with the simulated concentration distribution. Also, all the concentration profiles at the cross sections shown in Fig. 4 show close agreement with the Gaussian plume. However, there is some divergence from the purely Gaussian case. This is probably a consequence of the averaging from the numerical simulations. It takes a lot of ensembles to get pure Gaussian plots in experiments and numerical simulations.

Figures 5 and 7 show the time-averaged concentration fields for cases 2 and 3 shown in Table 1, respectively. The pen-induced drag coefficient for case 2 is $C_D = 0.5$ and for case 3, $C_D = 1$. It is evident that the plume spread is enhanced by the drag induced by the pen for both cases. Rummel et al. [17] also observed enhanced plume growth (similar to

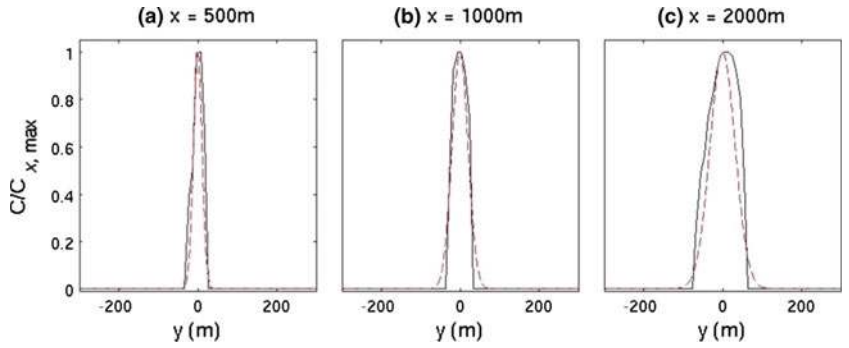

Fig. 4 Time-averaged concentration distributions (*solid lines*) at **a** $x = 500$ m, **b** $x = 1000$ m and **c** $x = 2000$ m. The *red dashed lines* are the Gaussian profiles calculated using a transverse mixing coefficient of $0.03\,\mathrm{m^2\,s^{-1}}$, for the steady uni-directional test flow case shown in Fig. 3

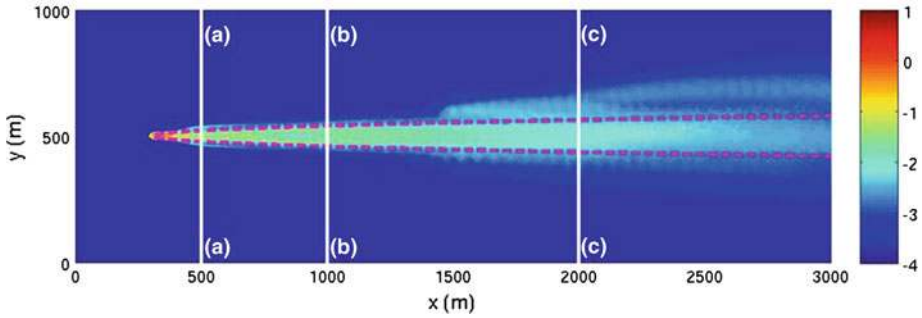

Fig. 5 Time-averaged normalized concentration field (shown in color) for case 2 shown in Table 1. The *dashed red line* shows the classical spread of a Gaussian plume using a lateral diffusivity of $0.03\,\mathrm{m^2\,s^{-1}}$

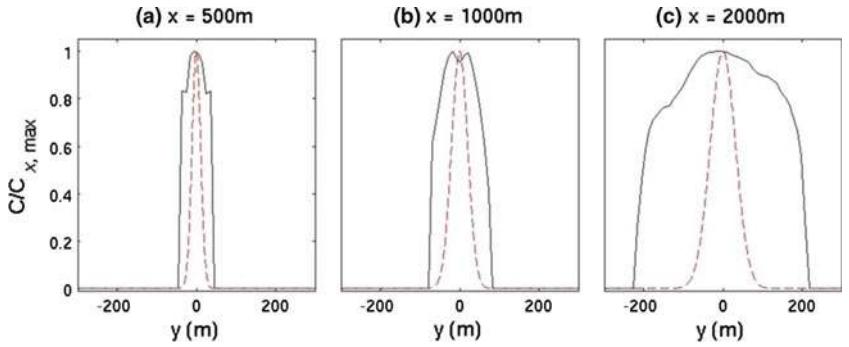

Fig. 6 Time-averaged concentration distributions (*solid lines*) for case 2 shown in Fig. 5 at **a** $x = 500$ m, **b** $x = 1000$ m and **c** $x = 2000$ m. The *dashed red lines* are the Gaussian profiles calculated using a transverse mixing coefficient of $0.03\,\mathrm{m^2\,s^{-1}}$ for case 1

Figs. 5, 7) in their shallow free-surface flow with grid turbulence experiments. The corresponding spanwise concentration distributions at sections (a–a), (b–b) and (c–c) are shown in Figs. 6 and 8, respectively. These profiles highlight how the plumes in cases 2 and 3 (under the influence of pen-induced drag) begin to depart quite early (at $x = 500$ m) from the clas-

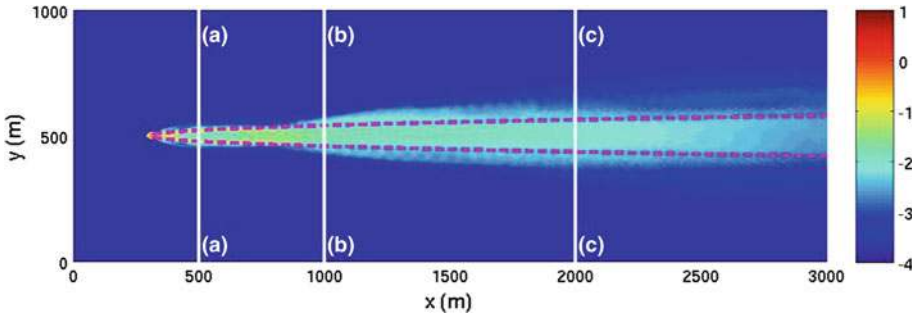

Fig. 7 Time-averaged normalized concentration field (shown in color) for case 3 shown in Table 1. The *dashed red line* shows the classical spread of a Gaussian plume using a lateral diffusivity of 0.03 $m^2\ s^{-1}$

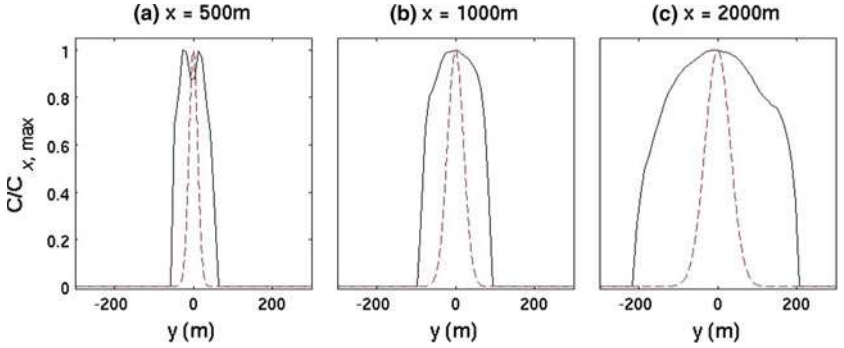

Fig. 8 Time-averaged concentration distributions (*solid lines*) for case 3 shown in Fig. 7 at **a** $x = 500$ m, **b** $x = 1000$ m and **c** $x = 2000$ m. The *dashed red lines* are the Gaussian profiles calculated using a transverse mixing coefficient of 0.03 $m^2\ s^{-1}$ for case 1

sical Gaussian plume. The plumes spread nearly twice as wide compared to the classical case (case 1) at $x = 2000$ m as shown in Figs. 6c and 8c, respectively. The average lateral diffusivities computed from the variances of the time-averaged concentration fields at the different cross sections are approximately 0.1 $m^2\ s^{-1}$ for case 2 and 0.15 $m^2\ s^{-1}$ for case 3, respectively. These values are about 3 to 5 times larger than the lateral mixing coefficient computed for case 1. This clearly shows the dramatic effect of the pen-induced drag on the plume dynamics. A higher value of the drag coefficient C_D results in a stronger vortex street that appears to enhance the lateral mixing considerably. *These results highlight the importance of accounting for the presence of the pens in plume dispersion calculations.*

Figure 9 shows the results of case 4. Here, the mixing and transport of a continuous point source scalar collocated within one fish pen is shown using a time sequence of the concentration field over a duration of nearly two tidal periods (with $T = 8$ h, $K = 46$, $\eta = 1$, $U_m = 0.1\ m\ s^{-1}$) under oscillatory flow conditions. When the tidal component is in phase with the mean current, the flow evolves in a similar manner to that of a uni-directional flow case (e.g. cases 2 and 3) with the usual formation of an unstable downstream wake resulting in vortex shedding (Fig. 9a, b). Soon after the initial vortex shedding begins, the flow starts to retard as the tidal velocity reverses direction and increases in amplitude. This causes the plume to contract in the longitudinal direction with a simultaneous dispersion in the lateral direction as shown in Fig. 9c, d, and during the subsequent tidal cycle in Fig. 9g, h, respectively. Note how

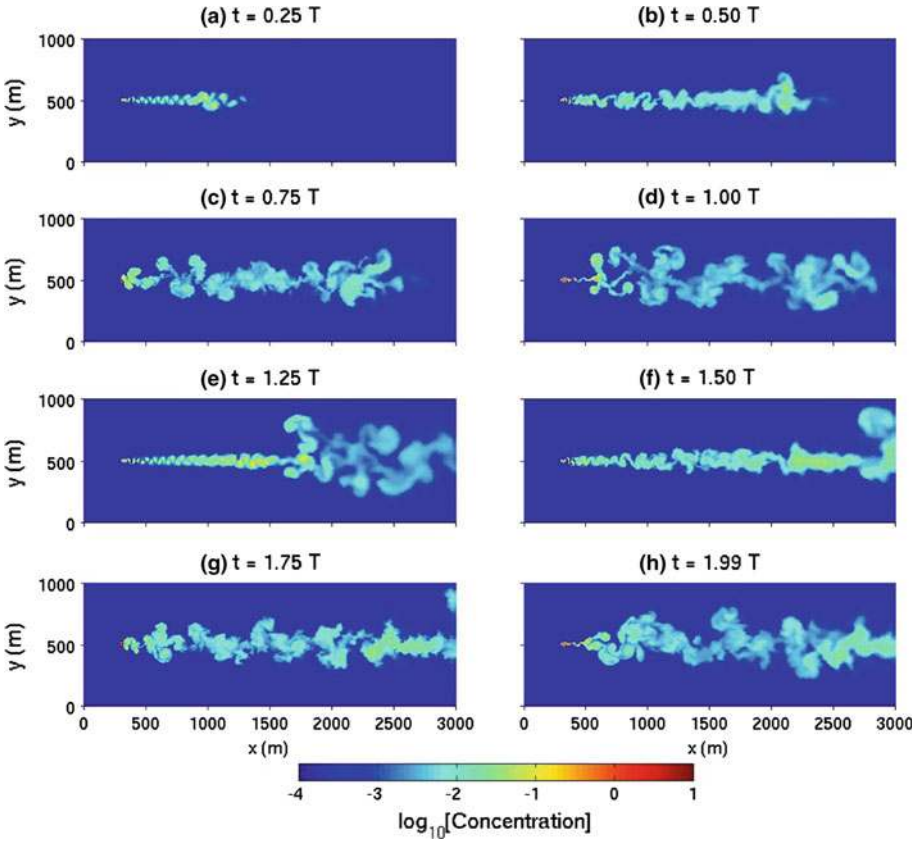

Fig. 9 Normalized concentration field (shown in color) for an oscillatory test flow case ($U_T / U_m = 1$, $K = 46$, case 4 in Table 1). The continuous point source is located within the perimeter of the fish pen. Time is normalized by the tidal period $T = 8$ h

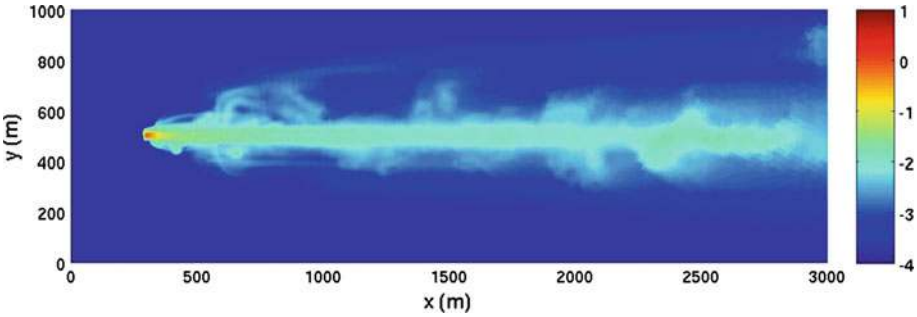

Fig. 10 Time-averaged normalized concentration field (shown in color) for an oscillatory test flow case (case 4 in Table 1) with $K = 46$ and $\eta = 1$

the vortex shedding is also attenuated during this period. This behavior was first described by Chatwin [4], where he points out that the contaminant cloud appears to be periodically expanding and contracting. The plume is stretched during the period of high flow during

the first half of the tidal cycle and contracts during the second half-cycle (see also [18]) The time-averaged concentration field is shown in Fig. 10, which clearly demonstrates the enhanced dispersion that occurs under oscillatory flow conditions compared to the classical dispersion (case 1) that would occur under uni-directional flow conditions. The slight asymmetry in the time-averaged concentration field in Fig. 10 is due to the finite number of tidal cycles over which the averaging is performed. This results in a distribution that is skewed in the direction of a set of counter-rotating vortices that emerge in the positive y-direction upon the first tidal reversal, as depicted in Figs. 9c, d. As shown in Figs. 9e, f, these counter-rotating vortices move in the positive y-direction, thereby causing a skew in the averaged concentration field. Subsequent ejections of counter-rotating vortices are not as strong and therefore, opposite-signed vortices do not counteract the effect of the first pair unless many more tidal cycles are computed. We should also note that the asymmetry is accentuated by the logarithmic concentration contours. Regardless, these results indicate that the mixing and dispersion of the pollutant field under oscillatory flow conditions with pen-induced drag is very different (and enhanced) from a classical uni-directional flow case without pen-induced drag (see Fig. 3). It is also worth noting that the plume growth in case 4 is further enhanced compared to cases 2 and 3, which indicates that the combined action of pen-induced drag and oscillations in the flow field is very effective in mixing the plume laterally. As a comparison, the spread of the plume at $x = 2000$ m for case 4 is almost twice as wide as that of case 3 at the same location.

3.2 Embayment results

Here, we present the results of all the embayment simulation cases presented in Sect. 2.3 and Table 1.

3.2.1 Offshore base case (case 5)

The passive scalar concentration field from a simulation run with two sets of fish farm pens located along the edge of the embayment is shown in Fig. 11 as a time sequence over a duration of six tidal periods. For this 'offshore base case', we have included the drag induced by each of the pens on the flow field and have also taken into account the earth6́s rotation. Using a Coriolis parameter of $f = 8.7 \times 10^{-5}$ rad s^{-1}, and the embayment width as the length scale, the Rossby number for this case is $R = U_m/fL = 0.26$, which indicates that the Coriolis force will likely influence the flow dynamics. The flow field is driven by a tidal flow from north to south combined with a southerly flowing mean current. The relevant oscillating flow parameters as shown in Table 1 are $\eta = 1$ and $K = 71$, based on a tidal velocity amplitude of $U_T = 0.1$ m s^{-1} and M_2 tidal period of 12.42 h. The formation of the downstream vortex shedding is evident early on as shown in Fig. 11a. As the flow reverses, the plume contracts in a similar manner to that observed for the channel flow test case shown in Fig. 9. The plume, while predominantly transported downstream (southwards) due to the rather strong mean current, also tends to spread eastward into the bay (see Fig. 11c–f).

Figure 12 shows the concentration distribution for all the offshore cases (cases 5–8) outlined in Table 1 at time $t = 4T$ to highlight the differences in the plume behavior between these cases. To assess the dispersion characteristics of the concentration plumes, we analyzed longitudinal profiles of the concentration along the coastline as shown in Fig. 13 at times

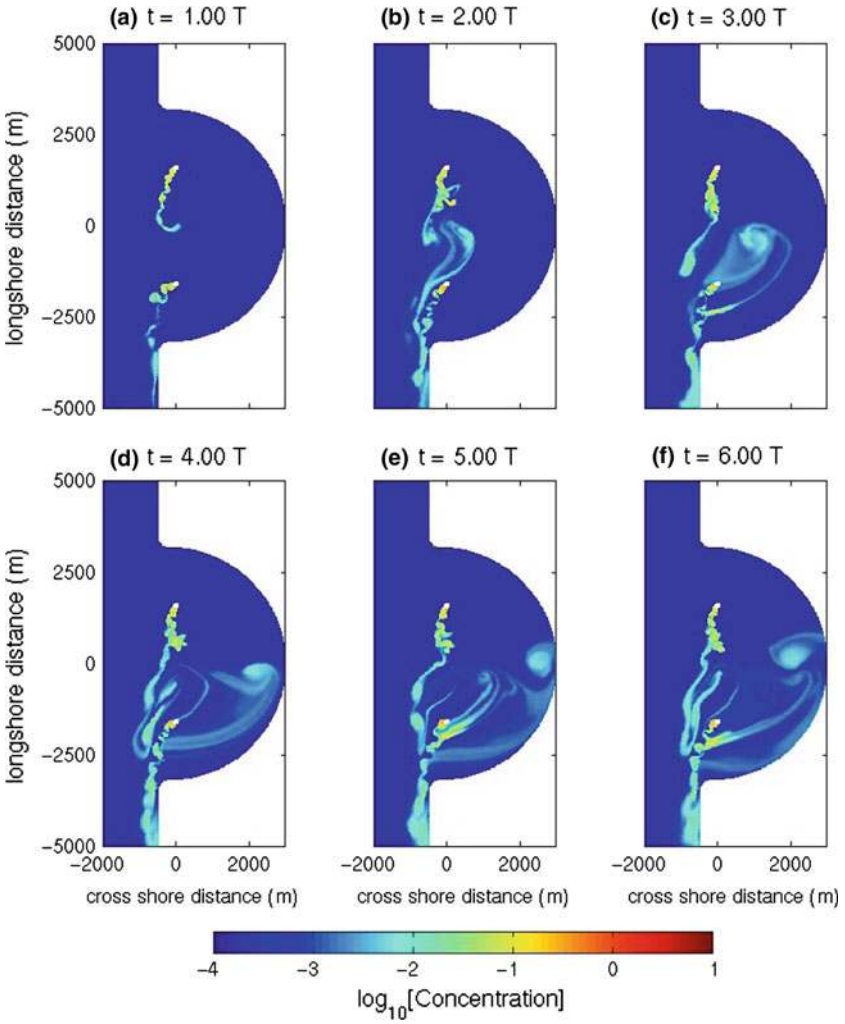

Fig. 11 "Birds-eye-view" of the time history of the normalized concentration in the vicinity if two sets of 6 20 m diameter pens (depicted as white boxes) releasing a passive scalar at the edge of the coastal embayment for the 'offshore base case' (case 5)

$t = 3T$ and $6T$, respectively. The alongshore concentrations profiles for cases 6, 7 and 8 are also shown in Fig. 13 for comparison. These profiles for the 'offshore base case' clearly show that the waste plume disperses toward the embayment coast albeit at very low concentration levels.

We computed the moments of the alongshore concentration distribution (as discussed in Sect. 2.4 for all the embayment cases) and the statistics are shown in Tables 2 and 3. Also shown in Tables 2 and 3 are the peak values of the concentration for all the embayment cases outlined in Table 1 at $t = 3T$ and $6T$, respectively. Time series of the concentration profiles at three locations along the embayment coastline highlight the temporal intermittency in the concentrations along the embayment coast (see Fig. 14). Details of the results of these simulations are discussed in what follows.

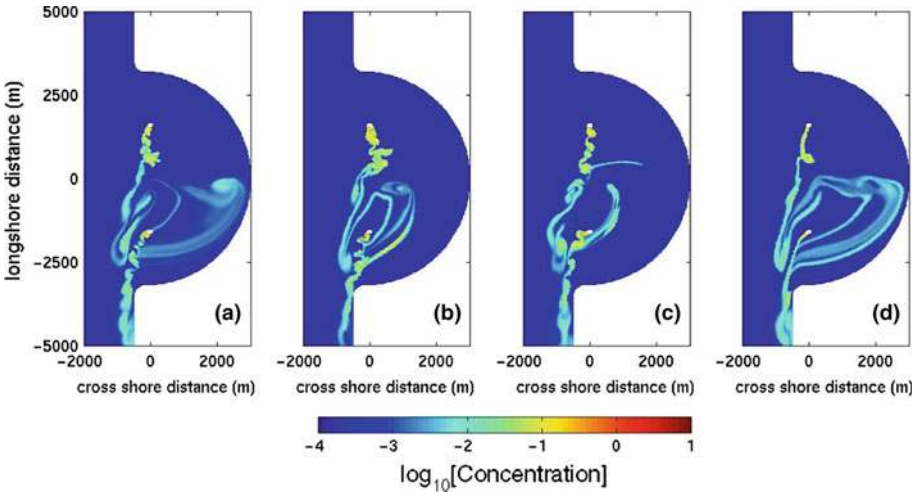

Fig. 12 "Birds-eye-view" of the time history of the normalized concentration in the vicinity if two sets of 6 20 m diameter pens (depicted as white boxes) releasing a passive scalar at the edge of the coastal embayment at time $t = 4T$ for **a** offshore base case (case 5), **b** offshore with no rotation case (case 6), **c** offshore with river inflow case (case 7), and **d** offshore with no pen drag case (case 8), respectively

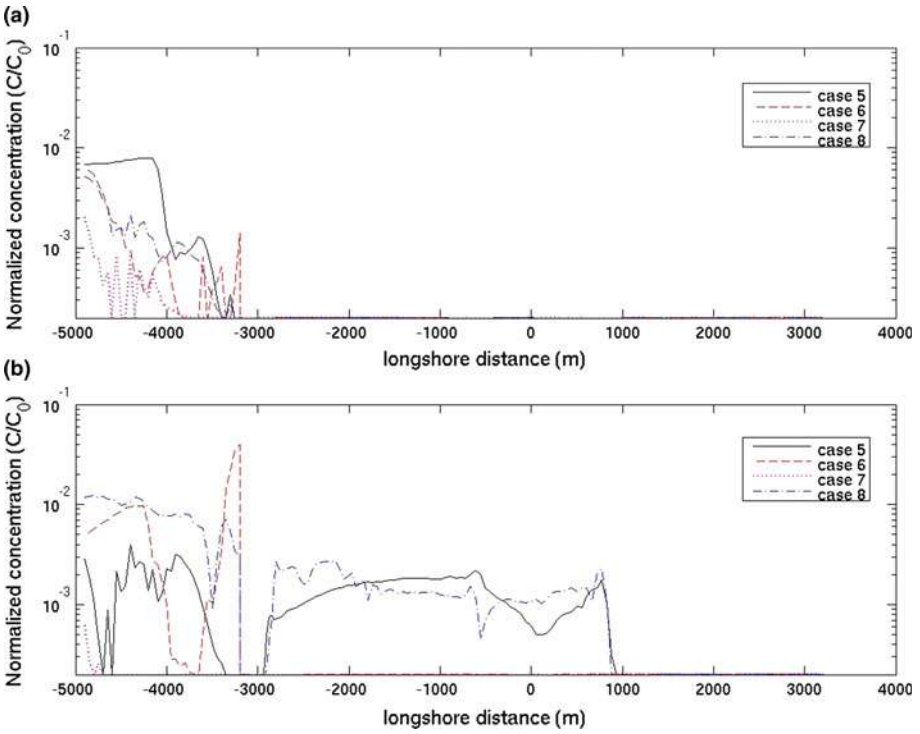

Fig. 13 Concentration profiles of the passive scalar along the embayment coast line at **a** $t = 3T$ and **b** $t = 6T$, for the 'offshore base case' (*solid line*, case 5), offshore with no rotation case (*dash line*, case 6), offshore with river inflow case (*dotted line*, case 7) and offshore with no pen drag case (*dash-dotted line*, case 8), respectively

Table 2 Statistics of the alongshore concentrations depicted in Figs. 13a and 17a at time $t = 3T$

Case #	Case name	Mean $\overline{C}$ ($\times 10^{-3}$)	Standard deviation σ ($\times 10^{-3}$)	Skewness γ	Kurtosis β	Peak value ($\times 10^{-3}$)
5	Offshore base case	0.61	1.92	3.06	10.58	7.73
6	Offshore with no rotation	0.18	0.78	5.66	36.41	5.69
7	Offshore with river inflow	0.04	0.17	7.18	63.86	1.83
8	Offshore with no pen drag	0.20	0.71	4.69	27.00	4.94
9	Nearshore base case	0.05	0.15	3.64	15.96	0.89
10	Nearshore with strong tides	0.00	0.00	10.24	111.52	0.00
11	Nearshore with wind	0.87	3.00	5.43	34.96	21.26

Table 3 Statistics of the alongshore concentrations depicted in Figs. 13b and 17b at time $t = 6T$

Case #	Case name	Mean $\overline{C}$ ($\times 10^{-3}$)	Standard deviation σ ($\times 10^{-3}$)	Skewness γ	Kurtosis β	Peak value ($\times 10^{-3}$)
5	Offshore base case	0.62	0.77	1.11	3.69	3.74
6	Offshore with no rotation	1.09	4.36	6.25	48.66	39.92
7	Offshore with river inflow	0.00	0.00	13.71	195.37	0.41
8	Offshore with no pen drag	1.81	3.10	2.11	6.29	12.07
9	Nearshore base case	2.78	4.52	1.76	5.20	21.80
10	Nearshore with strong tides	0.34	1.21	4.85	28.36	8.92
11	Nearshore with wind	2.36	4.38	2.32	8.13	21.43

3.2.2 Offshore case without rotation (case 6)

The effect of the earth's rotation on the dispersion of the plume was investigated by simply switching off the Coriolis term in (1) and (2) in our numerical code. Figure 12b shows the concentration field at time $t = 4T$ together with the concentration field for 'offshore base case' for the same time (Fig. 12a). For this scenario, it is seen that the plume does not spread deep into the embayment. The kurtosis of the alongshore concentration distribution for this case are considerably higher than the 'offshore base case' as shown in Tables 2 and 3. The absence of the Coriolis force implies that the flow field is not deflected into the embayment especially during slack tides when the effects of rotation are expected to be very strong. Hence, when the tide turns, the plume is flushed downstream (southwards) with much higher concentrations as indicated by the high peak in Fig. 13b at $t = 6T$, resulting in a highly peaked distribution. Furthermore, the asymmetry in the concentration distribution is also enhanced by the absence of the Coriolis forcing as indicated by skewness statistics in Tables 2 and 3. *These results clearly demonstrate that the large scale effect of the earth's rotation does indeed influence the dispersion of such plumes and should not be disregarded in numerical modeling*.

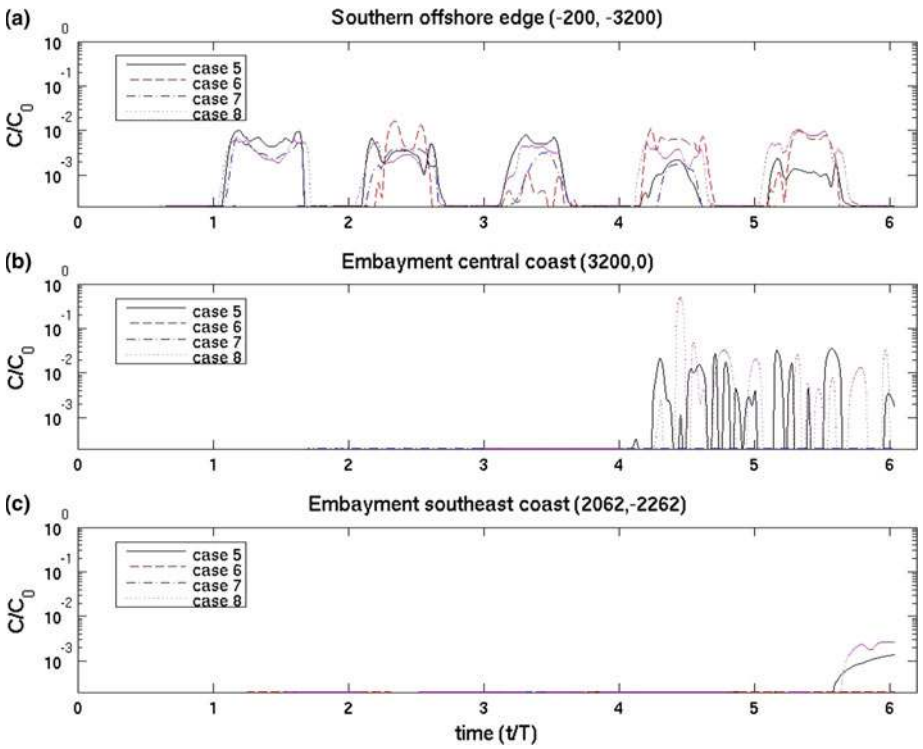

Fig. 14 Time series of concentration profiles of passive scalar at three different locations along the embayment coast for offshore cases 5 (*solid line*), 6 (*dash line*), 7 (*dash-dotted line*), and 8 (*dotted line*), respectively

3.2.3 Offshore case with river inflow (case 7)

Enclosed coastal embayments may often have rivers discharging into them. A small inflow river discharge with a velocity of $U_R = 0.05\,\mathrm{m\,s^{-1}}$ was placed at the head of the channel incision as discussed in Sect. 2.3. The resulting plume concentration at $t = 4T$ is shown in Fig. 12c. With all other parameters being equal with the 'offshore base case', it is evident (as would be expected) that the plume spread into the embayment is impeded by the river inflow. Both the skewness and kurtosis of the concentration distributions alongshore are considerably higher than the 'offshore base case'. However, in contrast to the previous case (no rotation case), the time sequence of the plume distributions (not shown here) clearly indicate that the plume does not hug the embayment coast except further downstream resulting in a highly skewed distribution. *This is clearly a desirable situation for fishfarm operations since the waste plume is very unlikely to reach the coastline due to the flushing action of the freshwater inflow*. For a buoyant river plume, further research using three-dimensional simulations are required to capture the vertical mixing of the river plume with the denser coastal water.

3.2.4 Offshore case with no drag (case 8)

The effect of the drag induced by the fish pens causes flow separation and vortex shedding thus enhancing the local mixing as was clearly demonstrated from the results of the

open channel test cases (cases 2 through 4). In an effort to understand the influence of blockage introduced by the pens, we ran an 'offshore case' without accounting for the drag from the pens. For this case, it is clear from the concentration distribution shown in Fig. 12d that the absence of drag results in less mixing compared to the 'offshore case' shown in Fig. 12a, even though the overall plume distribution looks very similar. The peak concentration is at least three times higher than the peak value for the 'offshore base case' as shown in Table 3 at $t = 6T$. *This result in conjunction with the results of the channel flow test cases (cases 2–4) highlights the need to correctly account for the drag induced by the pens in predictive numerical models for water quality applications*. An over prediction of the drag

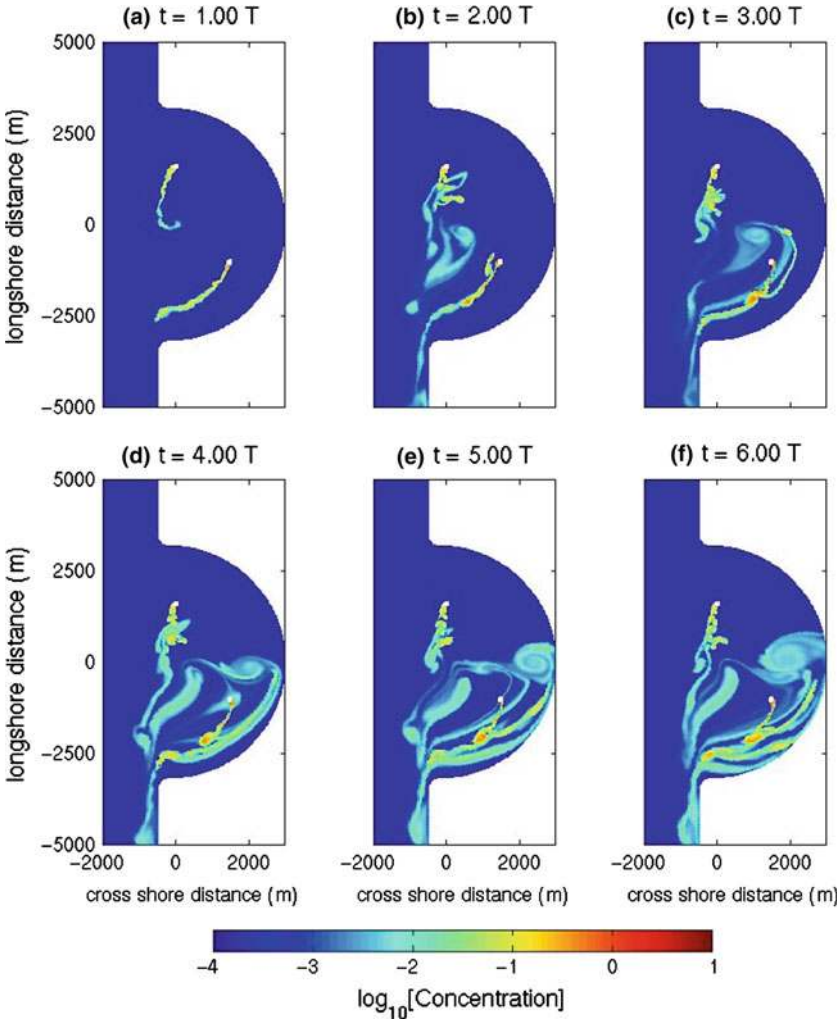

Fig. 15 "Birds-eye-view" of the time history of the normalized concentration in the vicinity if two sets of 6 20 m diameter pens (depicted as white boxes) releasing a passive scalar at the edge of the coastal embayment for the 'nearshore base case' (case 9)

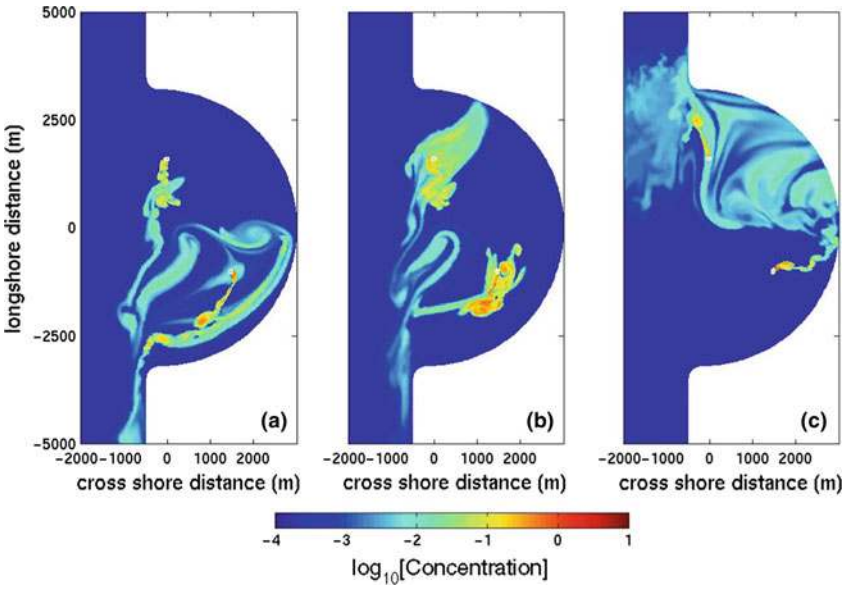

Fig. 16 "Birds-eye-view" of the time history of the normalized concentration in the vicinity if two sets of 6 20 m diameter pens (depicted as white boxes) releasing a passive scalar at the edge of the coastal embayment at time $t = 4T$ for **a** nearshore base case (case 9), **b** nearshore with strong tides case (case 10), **c** neashore with wind case (case 11), respectively

(i.e. a higher drag coefficient) will result in a well mixed plume and on the other hand, under prediction (i.e. a lower drag coefficient) of the drag will imply poor mixing conditions.

3.2.5 Nearshore base case (case 9)

We have thus far presented results based on two sets of fish farms pens located along the edge of the embayment as shown in Fig. 1. For cases 9, 10 and 11, the southern facing farm in Fig. 1 was moved into the bay and closer to the channel incision. The concentration distributions of the plume for case 9 as seen in Fig. 15 indicate much higher concentrations closer to the coast compared to the 'offshore base case' (case 5). Figure 16 shows the concentration distributions at time $t = 4T$ for all the nearshore cases (cases 9, 10 and 11, respectively). As expected, the concentration profiles along the coast as shown in Fig. 17 are at least an order of magnitude higher than those for the 'offshore base case' (Fig. 13) especially at $t = 6T$. Time series of the concentrations at the three same locations shown for all offshore cases in Fig. 14 are repeated here for all the nearshore cases (see Fig. 18). The relocation of the farm close to the coast has reduced the concentration at the southern offshore boundary (Fig. 16a) while the concentration at the head of the channel incision has dramatically increased by up to two orders of magnitude (Fig. 16b).

3.2.6 Nearshore case with $\eta = 2$ (case 10)

The parameter η given in Eq. 6 determines the shape of the plume. In other words, it quantifies the effect of the tidal action to that of the mean current. A higher value of η signifies a stronger tidal signal and allows for a stronger plume reversal. A simulation for the 'nearshore

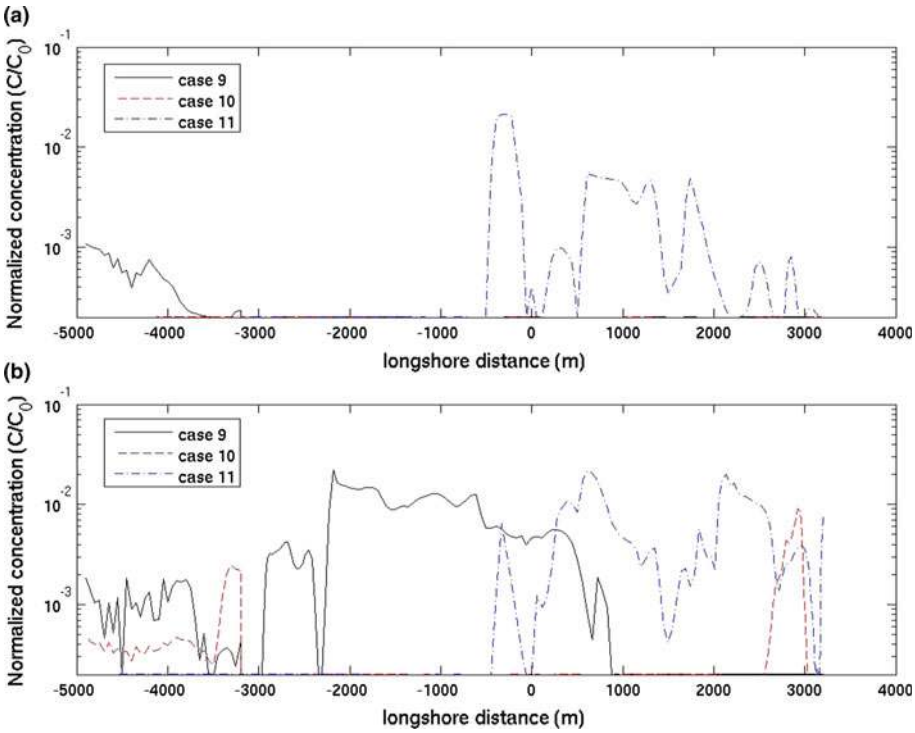

Fig. 17 Concentration profiles of the passive scalar along the embayment coast line at **a** $t = 3T$ and **b** $t = 6T$, for the 'nearshore case' (*solid line*, case 9), nearshore case with strong tides (*dash line*, case 10), and nearshore case with wind (*dash-dotted line*, case 11), respectively

case' was performed with $\eta = 2$ with the results of the concentration distribution shown in Fig. 16b. We see dramatic changes in the plume structure for this case compared to the distribution for the 'nearshore base case' shown in Fig. 16a. The plume undergoes a much stronger reversal as the tide changes direction. It is clear from this figure (and other time sequence plots not shown here) that the plume reaches some parts of the northern coast. The strong sloshing motion of the tidal flow in the alongshore direction results in highly peaked and skewed distributions compared to the 'nearshore base case' as shown by the high values of the kurtosis and skewness in Tables 2 and 3. *This result indicates the importance of identifying the correct (and dominant) hydrodynamic conditions at a particular fish farm site because these conditions will dramatically influence how far a waste plume from a fish farm site would spread.*

3.2.7 Nearshore case with surface wind stress (case 11)

Finally, we present a 'nearshore case' with a surface wind stress acting over the entire embayment in the northerly direction (i.e. opposite to the tidal flow). We have also removed the mean current for this case in order to explore the effect of the wind-induced circulation on the plume distribution. Figure 16c shows the concentration distribution at $t = 4T$. The pattern for this case is completely different to those shown earlier. Here, the wind stress used was estimated to yield a mean velocity of $0.1\,\mathrm{m\,s^{-1}}$ based on a mean wind speed $U_{10} = 10\,\mathrm{m\,s^{-1}}$

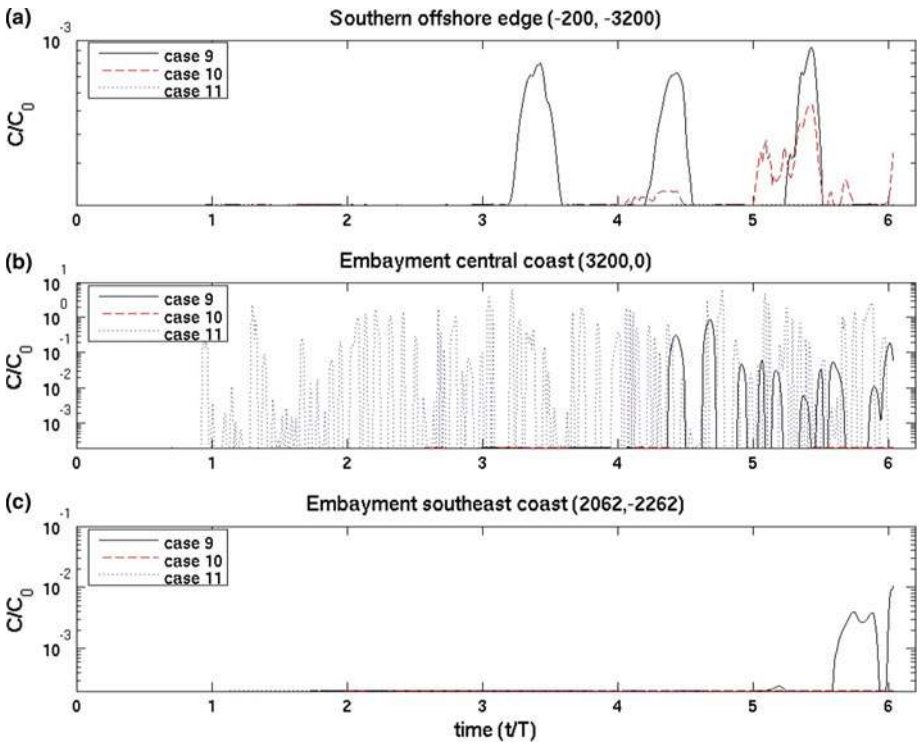

Fig. 18 Time series of concentration profiles of passive scalar at three different locations along the embayment coast for nearshore cases 9, 10, and 11, respectively

at a height of 10 m in the atmospheric boundary. Clearly, it is seen that the wind effect is dominant and tends to drive the distribution in a northward direction. This is accentuated even more when the tide reverses and the plume is dispersed more toward the northern end of the bay.

4 Conclusions

This study presents results from highly-resolved two-dimensional, depth-averaged numerical simulations of the mixing and transport of continuous point sources of waste from an array of aquaculture pens modeled as porous cylinders. The results highlight the complex and different dispersion patterns that occur under such flow conditions. In particular, the results from this study demonstrate the following key points:

– The mixing and dispersion of the pollutant field under oscillatory flow conditions with added drag from the fish pens is very different from the classical uni-directional flow case where a Gaussian plume spread occurs. Under oscillatory flow conditions, our results show plumes of waste with relatively high concentration occurring at considerable distances from the source.
– The large scale effect of the Earth's rotation does indeed influence the dispersion of contaminant plumes and should be accounted for in numerical models.

– The local runoff from rivers and other tributaries should be taken into account in modeling the plume dispersion in near-coastal environments.
– Accounting for the drag induced by the pens is important to accurately predict the level of mixing in numerical models for water quality applications.
– It is necessary to identify the correct (and dominant) hydrodynamic conditions at a particular fish farm site because these conditions will dramatically influence how far a waste plume from a fish farm site would spread.

In addition, our work shows strong "non-Gaussian" behavior in that the spatial decay is not necessarily exponential. This is highlighted by the statistics of the plume concentrations, which indicate highly peaked and skewed distributions and *show that high concentrations of the scalar field can be found at significant distances from the source*. The results also indicate pronounced spatio-temporal variability in the concentration fields and this spatio-temporal variability is a strong function of the particular forcing parameters involved. *Based on our results, "dilution as a solution to pollution" should not be prescribed for marine aquaculture, particularly in near-shore systems*.

This study is a first step towards understanding the complex plume dispersion dynamics in the vicinity of aquaculture farms in nearshore coastal waters. Further work using three-dimensional simulations, is required to gain key insights into the three-dimensional flow structure that would occur in the close proximity of aquaculture pens. As an extension to this study, we are performing highly-resolved, three-dimensional, nonhydrostatic simulations to understand the plume structure resulting from the complex flow pattern that occurs due to flow separation over and under submerged pens under stratified flow conditions. We also plan to couple the flow model with a biological model that will allow for the prediction of other water quality parameters, such as dissolved oxygen and plankton concentrations. The use of such models in the design of water quality regulations and the monitoring of wastes will be key to ensuring an environmentally sound aquaculture industry.

Acknowledgments We thank the three anonymous reviewers for their constructive comments and recommendations which were very helpful in improving both the content and clarity of this paper. This work was supported by Lenfest Ocean Program (Program director: Margaret Bowman). We gratefully acknowledge Jerry Harris and Dennis Michael for providing time on the Stanford CEES cluster. SKV also gratefully acknowledges start-up support funds from the Department of Civil and Environmental Engineering (Head—Professor Luis Garcia) at Colorado State University.

References

1. Bowden KF (1967) Stability effects on turbulent mixing in tidal currents. Phys Fluids Supp 10:S278–S280
2. California Fish and Game Code Sec.15008 (2006)
3. California Regional Water Quality Control Board, Central Coast Region (2002) Waste Discharge Requirements NPDES General Permit for Discharges from Aquaculture and Aquariums. Order no. R3-2002-0076
4. Chatwin PC (1975) On the longitudinal dispersion of passive contaminant in oscillatory flow in tubes. J Fluid Mech 71:513–527
5. Crimaldi JP, Wiley MB, Koseff JR (2002) The relationship between mean and instantaneous structure in turbulent passive scalar plumes. J Turbul 3(014). http://stacks.iop.org/JoT/3/014
6. Delaux S, Stevens CL, Popinet S (2010) High-resolution computational fluid dynamics modelling of suspended shellfish structures. Environ Fluid Mech. doi:10.1007/s10652-010-9183-y
7. Fischer HB, List EJ, Koh RC, Imberger J, Brooks NH (1979) Mixing in inland and coastal waters. Academic Press, San Diego
8. Fringer OB, Gerritsen MG, Street RL (2006) An unstructured-grid, finite-volume, nonhydrostatic, parallel coastal ocean simulator. Ocean Modell 14:139–173
9. Helsley CE, Kim JW (2005) Mixing downstream of a submerged fish cage: a numerical study. IEEE J Ocean Eng 30(1):12–19

10. Hoyas S, Jiménez J (2006) Scaling of the velocity fluctuations in turbulent channel up to $Re_\tau = 2003$. Phys Fluids 18(7):011702
11. Jachec SJ, Fringer OB, Gerritsen MG, Street RL (2006) Numerical simulation of internal tides and the resulting energetics within Monterey Bay and the surrounding area. Geophys Res Lett 33. doi:10.1029/2006GL026314
12. Lau YL, Krishnappan BG (1977) Transverse dispersion in rectangular channels. J Hydraul Eng ASCE 103(10):1173–1189
13. Naylor R (2006) Environmental safeguards for open ocean aquaculture. Natl Acad Sci Issues Sci Technol (Spring) 53–58
14. Naylor R, Burke M (2005) Aquaculture and ocean resources: raising tigers of the sea. Annu Rev Environ Resour 30:185–218
15. Plew DR, Spigel RH, Stevens CL, Nokes RI, Davidson MJ (2006) Stratified flow interactions with a suspended canopy. Environ Fluid Mech 6:519–539
16. Purnama A, Kay A (1999) Effluent discharge into tidal water: optimal or economic strategy?. Environmetrics 10:601–624
17. Rummel AC, Socolofsky SA, Carmer CFv, Jirka GH (2005) Enhanced diffusion from a continuous point source in shallow free-surface flow with grid turbulence. Phys Fluids 17(7):075105
18. Smith R (1982) Contaminant dispersion in oscillatory flows. J Fluid Mech 114:379–398
19. Stacey MT, Cowen EA, Powell TM, Dobbins E, Monismith SG, Koseff JR (2000) Plume dispersion in a stratified, near-coastal flow: measurements and modeling. Cont Shelf Res 20(6):637–663
20. Stevens C, Plew D, Hartstein N, Fredriksson D (2008) The physics of open-water shellfish aquaculture. Aquacult Eng. 38(3):145–160
21. Wang B, Fringer OB, Giddings SN, Fong DA (2009) High-resolution simulations of a macrotidal estuary using SUNTANS. Ocean Modell 28(1–2):167–192
22. Zhang Z, Fringer OB (2006) A numerical study of nonlinear internal wave generation in the luzon strait. In: Proceedings of the 6th international symposium on stratified flows, pp 300–305